

Exceptional ballistic transport in epitaxial graphene nanoribbons

Jens Baringhaus^{1*}, Ming Ruan^{2*}, Frederik Edler¹, Antonio Tejada^{3,4}, Muriel Sicot³, AminaTaleb-Ibrahimi⁴, An-Ping Li⁵, Zhigang Jiang², Edward H. Conrad², Claire Berger^{2,6}, Christoph Tegenkamp¹ & Walt A. de Heer²

Graphene nanoribbons will be essential components in future graphene nanoelectronics¹. However, in typical nanoribbons produced from lithographically patterned exfoliated graphene, the charge carriers travel only about ten nanometres between scattering events, resulting in minimum sheet resistances of about one kilohm per square^{2–5}. Here we show that 40-nanometre-wide graphene nanoribbons epitaxially grown on silicon carbide^{6,7} are single-channel room-temperature ballistic conductors on a length scale greater than ten micrometres, which is similar to the performance of metallic carbon nanotubes. This is equivalent to sheet resistances below 1 ohm per square, surpassing theoretical predictions for perfect graphene⁸ by at least an order of magnitude. In neutral graphene ribbons, we show that transport is dominated by two modes. One is ballistic and temperature independent; the other is thermally activated. Transport is protected from back-scattering, possibly reflecting ground-state properties of neutral graphene. At room temperature, the resistance of both modes is found to increase abruptly at a particular length—the ballistic mode at 16 micrometres and the other at 160 nanometres. Our epitaxial graphene nanoribbons will be important not only in fundamental science, but also—because they can be readily produced in thousands—in advanced nanoelectronics, which can make use of their room-temperature ballistic transport properties.

The energy spectrum of a graphene ribbon with length L and width W is approximately given by

$$E_{n,m} = \pm \hbar c^* \sqrt{\left(\frac{n\pi}{W}\right)^2 + \left(\frac{m\pi}{L}\right)^2} \quad (1)$$

where $c^* \approx 10^6 \text{ m s}^{-1}$ is the Fermi velocity and \hbar is Planck's constant divided by 2π . For reference, if $W = 40 \text{ nm}$ and $L = 1 \mu\text{m}$, then $E_{1,0}/k_B = 600 \text{ K}$ and $E_{0,1}/k_B = 23 \text{ K}$, where k_B is Boltzmann's constant⁹. Following the Landauer equation¹⁰, the conductance G of a long graphene ribbon, measured in a two-probe measurement, is $G = 4G_0 \sum \text{Tr}_n$ where $G_0 = 1/R_0 = e^2/h$, and $0 \leq \text{Tr}_n \leq 1$ is the corresponding transmission coefficient (e is the electronic charge). At low temperatures for $|E_{n,0}| \leq |E_F|$, $\text{Tr}_n \approx (1 + L/\lambda_n)^{-1}$, where λ_n is the mean free path and E_F is the Fermi energy¹⁰. For $|E_{n,0}| > |E_F|$, $\text{Tr}_n = 0$. The $n = 0$ modes are special, and relate to edge states^{11,12}. They dominate transport when $|E_F| < |E_{1,0}|$, that is, for charge-neutral ribbons with temperature $T < 600 \text{ K}$. By analogy with high-quality carbon nanotubes¹³, charge-neutral low-defect graphene ribbons were expected to be micrometre-scale ballistic conductors¹. However, in lithographically patterned exfoliated graphene ribbons, transport in the edge states is quenched due to disorder^{2–5} (Supplementary Fig. 2).

In contrast, well-aligned, single-crystal monolayer graphene sheets form spontaneously on silicon carbide (SiC) surfaces heated above $1,000^\circ\text{C}$. In the structured growth method⁶, graphene ribbons self-assemble on the sidewalls of steps that are etched into the (0001)

surface of electronics-grade SiC wafers^{6,7,14–16} (see Figs 1a and 2), so that no graphene patterning is required to produce nanosized ribbons. More precisely, to prepare the ribbons shown below, 20-nm-deep trenches were etched along the SiC [1100] direction. The samples in Fig. 2 were annealed at $1,600^\circ\text{C}$ for 15 min (ref. 7). The samples in Fig. 3 were heated at $1,300^\circ\text{C}$ in Ar ($4 \times 10^{-5} \text{ mbar}$), and then in ultrahigh vacuum (UHV) for 15 min at $1,100^\circ\text{C}$ (green dots, Fig. 3a) or at $1,150^\circ\text{C}$ (all others—see Supplementary Information). The natural-step ribbon⁷

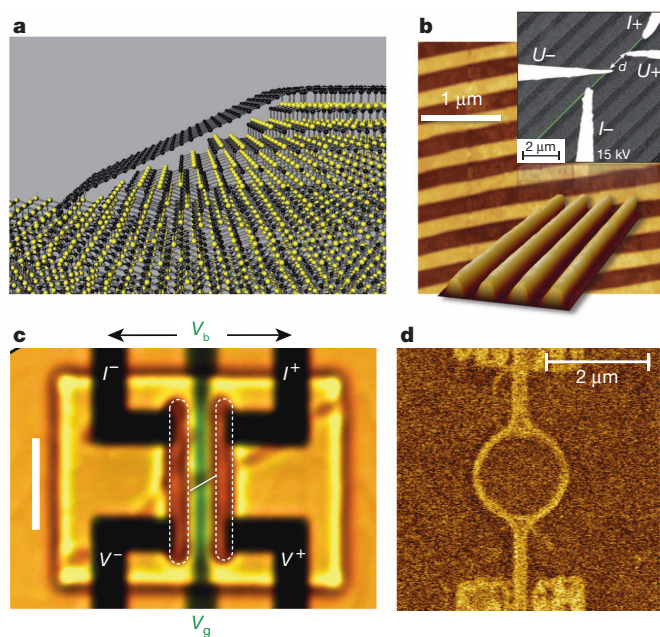


Figure 1 | Structure and characterization of nanoribbons and devices.

a, Schematic diagram of a graphene ribbon (all black) on an annealed and faceted sidewall (yellow and black; see ref. 17). **b**, AFM image of an array of graphene ribbons on sidewalls of 20-nm-deep trenches. Bottom inset, three-dimensional view, guided by an SEM, up to four individual probes are brought into contact with a selected graphene ribbon, and serve as current leads (I^+ , I^-) and voltage probes (V^+ , V^-). The sample can be transferred to and from an *in situ* heating stage for annealing up to $1,500^\circ\text{C}$. **c**, Optical micrograph of sidewall ribbon (sample A) supplied with leads and gate consisting of wide graphene ribbons ($1 \mu\text{m}$ apart) connected by a nominally 39-nm ribbon to form an H-shaped geometry, where the vertical, wide graphene ribbons serve as current leads (I^+ , I^-) and voltage probes (V^+ , V^-) for the $1.6\text{-}\mu\text{m}$ -long ribbon. White dashed lines indicate location of the graphene leads, white line indicates graphene ribbon. Green region locates the gate structure. Dark areas are the gold contacts. **d**, Electrostatic force image of a sidewall graphene nano-ring with $1.6\text{-}\mu\text{m}$ outer diameter attached to graphene leads. The ring is produced similarly to **c** and has graphene-covered sloping sidewalls.

¹Institut für Festkörperphysik, Leibniz Universität, Hannover, Appelstrasse 2, 30167 Hannover, Germany. ²School of Physics, Georgia Institute of Technology, Atlanta, Georgia 30332-0430, USA. ³Université de Lorraine, UMR CNRS 7198, Institut Jean Lamour, BP 70239, 54506 Vandoeuvre-lès-Nancy, France. ⁴UR1 CNRS/Synchrotron SOLEIL, Saint-Aubin, 91192 Gif sur Yvette, France. ⁵Center for Nanophase Materials Sciences, Oak Ridge National Laboratory, Tennessee 37831, USA. ⁶Institut Néel, CNRS UJF-INP, 38042 Cedex 6, Grenoble, France.

*These authors contributed equally to this work.

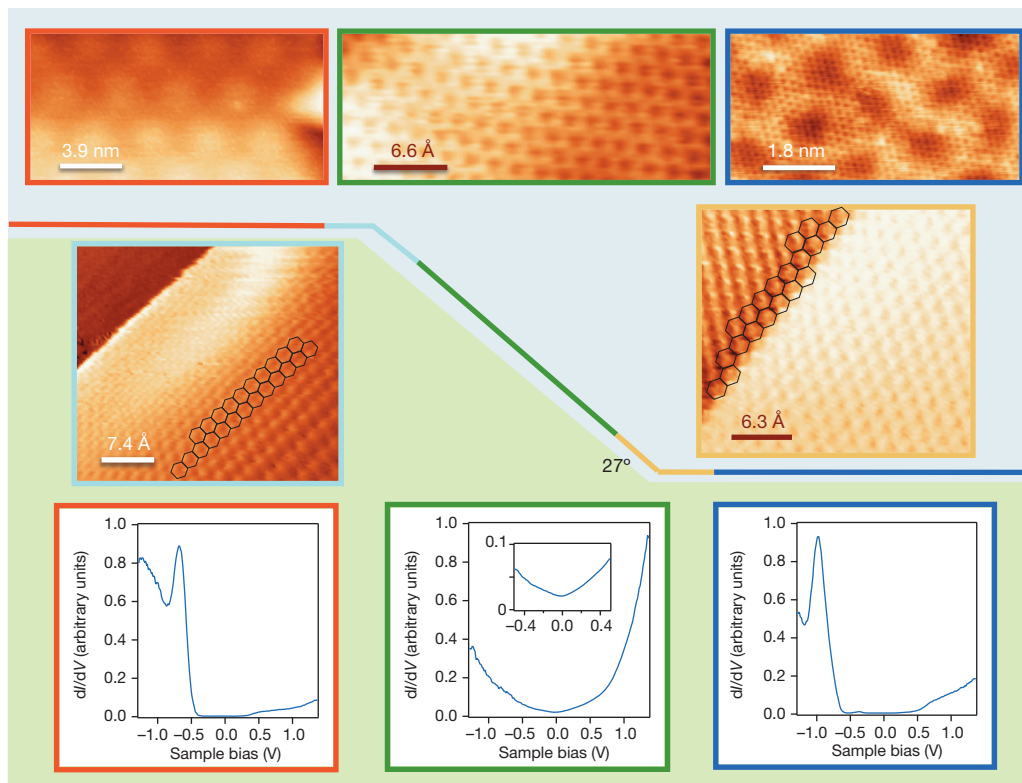


Figure 2 | Scanning tunnelling analysis of *ex situ* produced sidewall ribbons similar to those used in fixed geometry transport measurements. Colour-coded line over the 27° slope indicates areas of the surface investigated: colours correspond to the frame colours of the images. Top row: green frame shows atomic resolution STM of graphene structure on the sloped sidewall, and corresponds to the typical graphene STS traces shown in the bottom row (green

frame); red frame shows STM of upper terrace, blue frame shows STM of lower terrace. Middle row: blue frame shows STM of upper edge, and yellow frame shows STM of lower edge; both frames show helical edge structures. Bottom row: red and blue frames show STS of upper and lower terraces respectively, and show semiconducting gap.

(Figs 1c and 4) was connected at each end to two 200-nm-deep graphitized trenches 1 μm apart. These sidewall ribbons have been extensively characterized^{6,7,14–17} (Figs 1 and 2 and Supplementary Information) with scanning probe microscopies to determine ribbon widths and sidewall slopes. Angle-resolved photoemission spectroscopy (ARPES)¹⁶ performed at the Cassiopee beam line at the Soleil synchrotron shows a Dirac cone (Supplementary Fig. 1), demonstrating that the ribbons are well-aligned monolayers, and that the sidewall slope is uniform (that is, about 28°, consistent with the (2207) facet). Scanning tunnelling microscopy and scanning tunnelling spectroscopy (STM and STS) show that essentially charge-neutral graphene covers the sidewalls (Fig. 2). The top and bottom plateaus show the semiconducting properties of the ‘buffer layer’ (Fig. 2, red frames). Atomic-resolution images show zig-zag and chiral edges of the ribbons (Fig. 2).

Single-channel ballistic transport in epitaxial graphene ribbons was first reported^{7,15} on 40-nm-wide natural-step ribbons that were seamlessly connected to wide graphene leads (see Fig. 1c and Supplementary Information). These ribbons, used for the measurement presented in Fig. 4, were supplied with a top gate (20-nm Al_2O_3 coated with aluminium) so that E_F could be adjusted. Four wires were bonded to the graphene leads, facilitating four-point transport measurements.

Subsequently, we performed *in situ* variable-geometry transport measurements (at temperatures T from 30 to 300 K) on ~40-nm-wide ribbons (Fig. 1b), confirming single-channel ballistic transport as discussed below. Four nanoscopically sharp tungsten probes were positioned using a built-in scanning electron microscope and brought into ohmic electrical contact with a selected ribbon (Fig. 1b) in UHV (Omicron Nanoprobe UHV system). For two-probe (2p) measurements, a current I_{12} was passed between two probes, in contact with the ribbon, and the voltage V_{12} was measured so that $R_{2p} = V_{12}/I_{12}$. For four-probe

measurements, a current I_{34} was passed through outer probes and the potential difference V_{12} between the two inner probes (separated by a distance L) was measured: $R_{4p} = V_{12}/I_{34}$. The resistance per unit length R' is found from the slope of R_{4p} versus L for $1 \mu\text{m} \leq L \leq 16 \mu\text{m}$ (Fig. 3a). For these ribbons, R' ranges from 0 to $6 \text{ k}\Omega \mu\text{m}^{-1}$ (Fig. 1b). The R' values decrease after *in situ* heating (a process known to clean graphene), indicating that surface contamination increases scattering.

For these ribbons, both R_{4p} and R_{2p} extrapolate to $R \approx R_0 = h/e^2$ at $L = 0$ (Fig. 3a). Moreover, the resistivity ratio $\text{RR} = R_{4p}/R_{2p} = 0.95 \pm 0.02$. These results are characteristic of single-channel ballistic transport involving nearly perfectly invasive contacts^{10,18,19}. Furthermore, because an invasive probe acts as a scattering centre, R_{2p} is strongly modified if a third passive probe (with a very large resistance to ground) is placed between the contact probes¹⁰. Left-moving charges that enter the passive probe from the left, say, will leave the probe going either left or right with equal probability. Hence the transmission probability is $\text{Tr} = 0.5$ so that the overall wire resistance R_{2p} doubles from R_0 to $2R_0$ (see Supplementary Information). When two passive probes are used, the overall resistance R_{2p} increases to $3R_0$. From these considerations it follows that $\text{RR} = 1$ for perfectly invasive probes^{10,18,19}. This property of invasive probes is explicitly demonstrated in Fig. 3b. When one probe is placed on a ribbon, the end-to-end resistance R_{2p} increases from approximately R_0 to $2R_0$; when two probes are used, it increases to $3R_0$. Note that placing probes on a diffusive wire has no effect on the resistance of the wire. As shown in Fig. 3c, the resistance of these single-channel ballistic ribbons does not significantly depend on temperature or on the bias voltage.

For $0.1 \mu\text{m} \leq L \leq 1 \mu\text{m}$, $R(L)$ is found to increase nonlinearly from $0.5R_0$ to $1R_0$, as shown for two ribbons (Fig. 3a, upper left inset). For $L < L_{0-}^* = 160 \text{ nm}$, $R \approx R_0/2$, whereas for $L > L_{0-}^*$, R increases (see Fig. 3a upper left inset, and Supplementary Fig. 7). For the two ribbons,

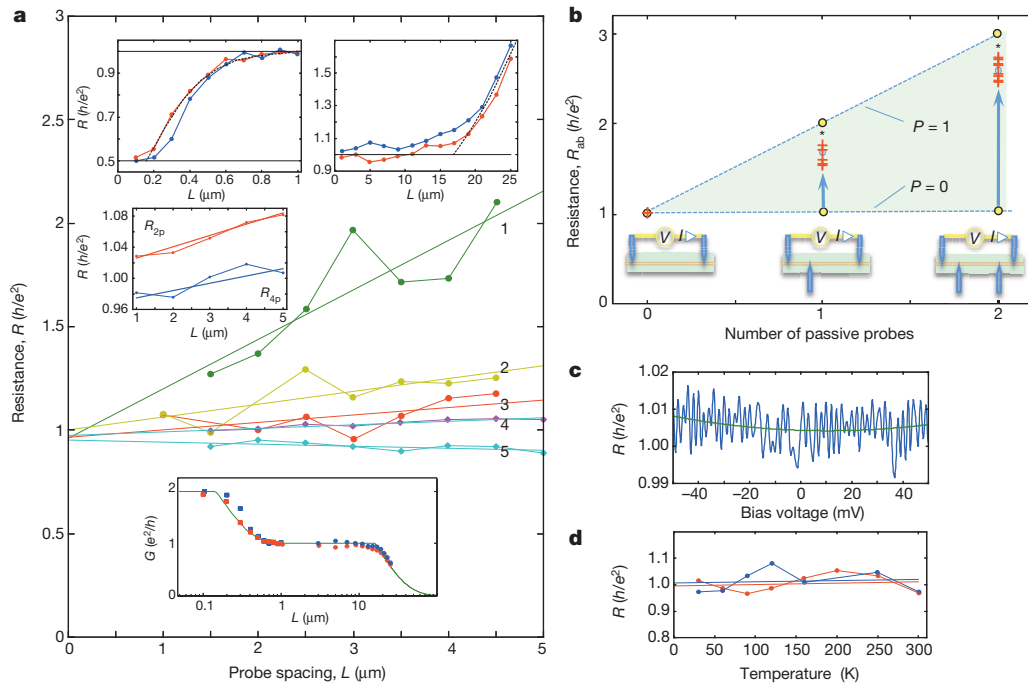


Figure 3 | Multiprobe *in situ* transport measurements of sidewall ribbons. **a**, Resistance versus probe spacing L . Linear fits extrapolate to $R_0 = h/e^2$. Slopes correspond to $R' = 6.2, 1.6, 0.92, 0.44 \text{ k}\Omega \mu\text{m}^{-1}$, corresponding to the mean free path $\lambda_0 = 4.2, 28, 16, 58 \mu\text{m}$ (following transmission $\text{Tr} \approx (1 + L/\lambda_0)^{-1}$). Line 5 is consistent with zero slope. Numbered traces are as follows: 1, UHV annealed at $1,100^\circ\text{C}$ for 15 min; 2, UHV annealed at $1,150^\circ\text{C}$ for 15 min; 3–5, re-annealed at $1,150^\circ\text{C}$ for 15 min. Middle inset, comparison of two-probe (2p) and four-probe (4p) measurements. Upper insets, nonlinear resistance increases observed at $L = 160 \text{ nm}$ and at $L = 16 \mu\text{m}$ in two different ribbons measured at room temperature, presented as $G(L)$ in the lower inset. Fit is

$R(L)$ was measured at 300 K from $1 \mu\text{m}$ to the apparatus limit, $L = 25 \mu\text{m}$ (Fig. 3a upper right inset). A second nonlinear increase is observed for $L > L_{0+}^* = 16 \mu\text{m}$. These nonlinearities are consistent with an exponential conductance decrease given by $G = G_0 \exp(1 - L/L_{0+}^*)$ for $L \geq L_{0+}^*$ as shown in Fig. 3a (dashed line in upper right inset). It is intriguing that $E_{01}^*/k_B = \pi\hbar c^*/L_{0+}^* = 150 \text{ K}$, suggesting that longitudinal excitations may be involved (equation (1)).

We next discuss the transport properties of a fixed-geometry sample (such as shown in Fig. 1c)⁷. Further examples are given in Supplementary Information. Sample A is a top-gated 39-nm-wide 1.6- μm -long graphene sidewall ribbon. The ribbon is seamlessly connected to micrometre-scale graphene pads to the left and right. Each pad is bonded to two wires, facilitating four-point transport measurements. Resistances around $20 \text{ k}\Omega$ are measured with better than 0.1Ω precision (corresponding to $\delta G < 5 \times 10^{-6} G_0$) using standard low-frequency lock-in techniques (13 Hz , $100 \text{ nA} < I < 1 \mu\text{A}$)⁷. Temperatures are measured with 2 mK precision. The charge density $n(V_g)$ is adjusted by applying a gate voltage, V_g ; we find that $n(V_g) = -0.95 \times 10^{12} V_g \text{ cm}^{-2} \text{ V}^{-1}$, as determined from a Hall bar on the same substrate⁷, so that $E_F = -0.11 V_g^{1/2} \text{ eV V}^{-1/2}$.

Figure 4c shows the conductance $G(V_g)$ as function of gate voltage for several temperatures, and can be globally explained in the Landauer picture with $\text{Tr}_n(E_F) = \text{Tr}_n \theta(|E_F| - |E_{n0}|)$ (θ is the step function)¹⁰. The minimum conductance $G = 0.95 G_0$ at $V_g \approx 0$ and $T = 4.2 \text{ K}$ is consistent with a single ballistic channel in charge-neutral graphene with $\lambda_{0+} = 22 \mu\text{m}$ (from $\text{Tr}_n \approx (1 + L/\lambda_n)^{-1}$). The conductance increase with increasing V_g corresponds to the opening of the $|n| \geq 1$ subbands²⁰, as diagrammatically shown in Fig. 4b. From the $G(V_g)$ slope we deduce that $T_{|n| \geq 1} = 0.035$, so that $\lambda_{|n| \geq 1} = 60 \text{ nm}$. We note that each of the curves can be displaced vertically to overlap the others. This is consistent with the Landauer picture and Fig. 3, if we assume that $T_{|n| \geq 1}$ is temperature independent and that only $T_{n=0-}$ is dependent

explained in main text. **b**, Effect of passive probes contacting sidewall ribbons. The resistance essentially doubles with one passive probe and triples with two passive probes. This property of ballistic conductors explains why four-probe and two-probe measurements yield essentially identical resistance values for ballistic wires. Ideal invasive probe ($P = 1$) and non-invasive probe ($P = 0$) limits are indicated. Theoretical^{18,19} values (for $\text{RR} = 0.95$) indicated by asterisks. **c**, Resistance R_{4p} of a typical ribbon for $L = 5 \mu\text{m}$ versus bias voltage V_b . **d**, Resistance versus temperature for the same ribbon, showing less than 10% variation from 30 K to 300 K .

on temperature, as indicated in Fig. 4b. (This subband-dependent temperature effect is also seen in exfoliated graphene ribbons, see Supplementary Fig. 2.)

Note that the large asymmetry with respect to V_g (Fig. 4a) is caused by the np/pn junctions (see, for example, ref. 21). For $V_g < 0$, the ribbon is p doped while the leads are slightly n doped^{7,16}. Because $\lambda_{|n| \geq 1} \approx 50 \text{ nm}$ is larger than the junction width, the junctions represent a significant barrier for the gapped $n \neq 0$ subbands; however, the ungapped $n = 0$ subbands are not affected²¹.

The conductance $G(T)$ increases monotonically with increasing temperature, as shown in Fig. 4e. In these experiments samples were cooled from 120 K to 4 K over 10 h, and two measurements were performed per second. The conductance is described to remarkable precision by

$$G(T) = \alpha \frac{e^2}{h} \left[1 + 0.5 \exp \left\{ - \left(\frac{T^*}{T_{\text{el}} - T_0} \right)^{1/2} \right\} \right] \quad (2)$$

where T_{el} is the effective electronic temperature (in this case, it is equal to the sample temperature), $\alpha = 0.922$, $T^* = 21.5 \text{ K}$ and $T_0 = 2.2 \text{ K}$. The difference $\delta G(T)$ between the fit and data is within $0.0015 G_0$ (0.1%) from $T = 4 \text{ K}$ to $T = 120 \text{ K}$ (Fig. 4e lower inset). Remarkably, the activation temperature T^* is related to the sample length L , with $T^* = 1.4\pi\hbar c^*/k_B L = 20.9 \text{ K}$ for $L = 1.6 \mu\text{m}$. Equation (2) applies to samples B, C and D (see Supplementary Information) as well. Specifically, for sample B (Supplementary Fig. 4), $\alpha = 0.31$ and the measured T^* is $T_m^* = 29 \text{ K}$; for $L = 1.06 \mu\text{m}$, the calculated T^* is $T_p^* = 1.4\pi\hbar c^*/k_B L = 31 \text{ K}$; for sample D (Supplementary Fig. 5), $\alpha = 0.63$ and $T_m^* = 87 \text{ K}$; for $L = 0.36 \mu\text{m}$, $T_p^* = 93 \text{ K}$. For the ring structure (Fig. 1d), $T_m^* = 6 \pm 1 \text{ K}$, and the measured contact-to-contact distance is $5 \mu\text{m}$ (following half a turn

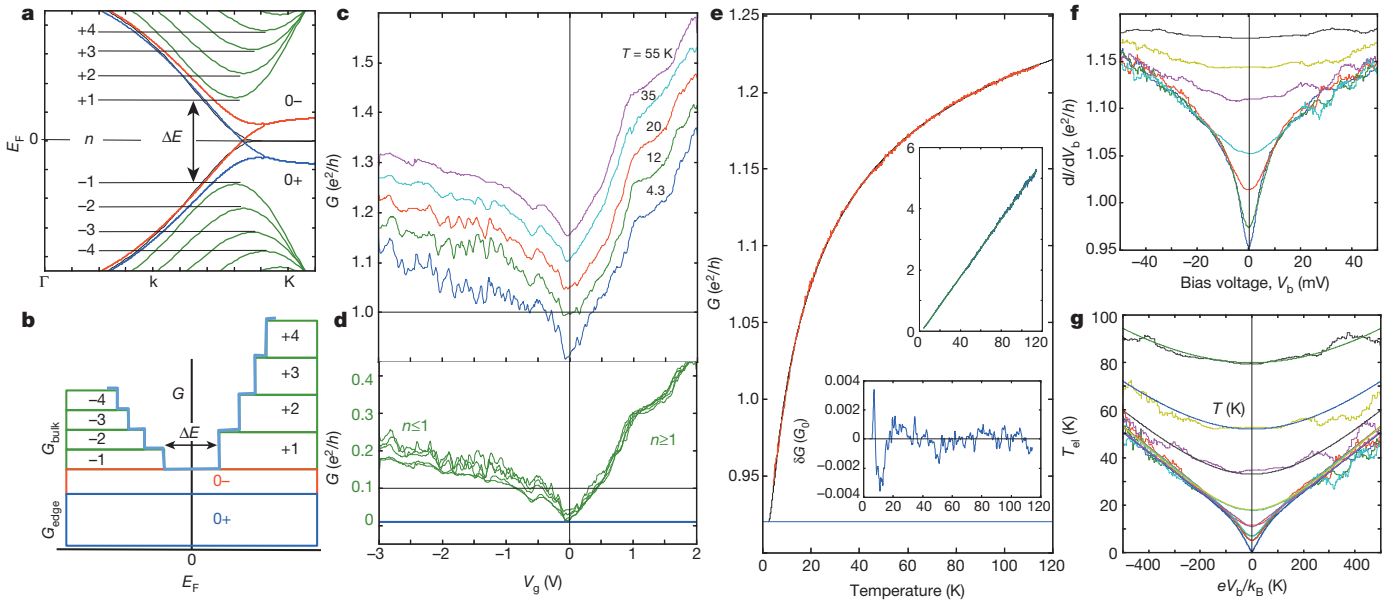


Figure 4 | Gated ribbon transport (see Fig. 1c). **a**, Schematic band structure. **b**, Conductance increase with increasing V_g is due to opening of subbands; for $|E_F| \leq E_1$, only the $n = 0 \pm$ subbands contribute; the conductance increase with increasing temperature is due to the $0-$ subband. **c**, Conductances $G_T(V_g)$ for various temperatures. Minimum conductance at $V_g = 0$ corresponds to charge-neutral ribbons ($E_F = 0$). **d**, Decomposition of $G_T(V_g) = G_{0+} + G_{0-}(T) + G_n(V_g)$. The $|n| \geq 1$ bands ($E_F \neq 0$) show no temperature dependence (apart from weak oscillations), as seen by the collapse of all the curves onto a single curve. **e**, Four-point G versus T (red curve)

of the circle), from which $T_p^* = 6.7$ K. This establishes the inverse L dependence of T^* in these samples (α and T^* appear to be unrelated), and implies that T^* is related to E_{01} (see equations (1) and (2)).

The increase of conductance with increasing bias voltage V_b (Fig. 4f) is attributed to electronic heating³. Using the conductance (equation (2)) as a thermometer allows us to determine $T_{el}(T, V_b)$ from the conductance. Moreover, we define $T_{vb} = eV_b/k_B$, to enable us to plot T_{el} versus T_{vb} , as shown in Fig. 4g. The data are fitted with:

$$T_{el} = \sqrt{T^2 + (T_{vb}/\nu)^2} \quad (3)$$

Figure 4g shows a good fit for all temperatures with the coefficient $\nu = 5$ for $T_{el} < 15$ K and $\nu = 12$ for $T_{el} > 15$ K. This behaviour is observed in samples B, C and D, and also in carbon nanotubes (Supplementary Figs 3, 4, 5, 6, 8).

Equation (2) resembles Mott's expression for one-dimensional variable range hopping²². It is therefore reasonable to expect a related mechanism. Following Mott's heuristic argument, charge carriers in disordered conductors ballistically hop from one scattering centre to the next, separated by a hopping distance L^* , following the path of least resistance, that is, one with the largest transmission coefficient. This transmission coefficient involves the product Z of two competing terms. One is the Boltzmann factor of the lowest longitudinal mode between the hopping endpoints, with activation energy $E_{01}^* = \pi\hbar c^*/L^*$, and the other is determined by the lifetime of the charge carrier τ . Consequently $Z = \exp(-E_{01}^*/k_B T) \exp(-t/\tau) = \exp(-\pi\hbar c^*/L^* k_B T) \exp(-L^*/c^* \tau)$, with t the carrier transit time over the distance L^* . We note that Z is a maximum for $L^* = \sqrt{(\pi\hbar c^* \tau / k_B T)}$, so that $Z = \exp(-\sqrt{T^*/T})$, where $T^* = 4\pi\hbar/k_B \tau$. From equation (2) and the inverse relation between T^* and L , we conclude that $\tau = 2.8L/c^*$, that is, of the order of (but larger than) the ballistic transit time through the ribbon. This rough estimate suggests that transport involves thermally activated longitudinal modes of the graphene ribbon. The dependence

superimposed on the theoretical curve from equation (2) (blue curve), showing an excellent fit. Upper inset, $[\ln(2G/\alpha G_0 - 2)]^{-2}$ versus T ; the inverse slope of the resulting line is $T^* = 21.5$ K and the zero intercept is $T_0 = 2.2$ K (equation (2)). Lower inset, difference $\delta G(T)$ between equation (2) and experiment. **f**, dI/dV_b versus bias voltage V_b ; from bottom to top, T (in K) is 4.2, 7, 12, 20, 35, 55, 80. **g**, Same data as in **f** plotted as a function of T_{el} ; $T_{el}(G)$ is determined from data in **e**, and $T_{vb} = eV_b/k_B$. Fits correspond to equation (3). For $T_{el} < 15$ K, $\nu = 5$; for larger T_{el} , $\nu = 10$.

on bias voltage indicates that impinging electrons produce hot charge carriers that overcome the activation barrier. The factor ν relates to the efficiency of this heating process.

The transport properties reported in Fig. 3 agree with those reported in Fig. 4, both showing two-component behaviour, each component contributing at most $1G_0$ to the conductance. The mean free path of the first component typically exceeds tens of micrometres and its resistance increases nonlinearly above $16 \mu\text{m}$. The second component is unusual. Transport is ballistic between scattering centres on the length scale L^* , which can be larger than the ribbon length L . Transport appears to be thermally activated with an activation barrier determined by the lowest longitudinal mode between the scattering centres (that is, E_{01}^*). This channel exhibits a positive linear magnetoconductance (discussed in Supplementary Information) that typically saturates at $B = 2$ T.

Room-temperature single-channel ballistic conduction in the $n = 0+$ mode was first observed two years ago in epitaxial graphene side-wall ribbons⁷. Single-channel ballistic transport in the $n = 0+$ channel is supported by the robust value of the quantum 'contact resistance' (at $L = 0$); the independence of the resistance with respect to length, temperature and bias voltage; the equivalence of two- and four-probe resistance measurements; and resistance doubling and tripling due to passive probes. Its insensitivity to gate voltages implies that this component is derived from a metallic subband¹³. Conduction in the $n = 0-$ mode appears to involve thermally activated transport (equation (2)) that is ballistic between widely spaced scattering centres. The separation of scattering centres can exceed the ribbon length in fixed geometry samples, where the ribbon is seamlessly connected to graphene leads. The activation barrier is found to be inversely proportional to the ribbon length. In addition, an energy gap equivalent to $T_0 = 2.2$ K appears to be involved. The conductance bias voltage dependence is explained in terms of electronic heating. Its insensitivity to gate voltages implies that it too is derived from a metallic subband. The $n = 0-$ mode also exhibits linear positive magnetoconductance. If the conductance increase is

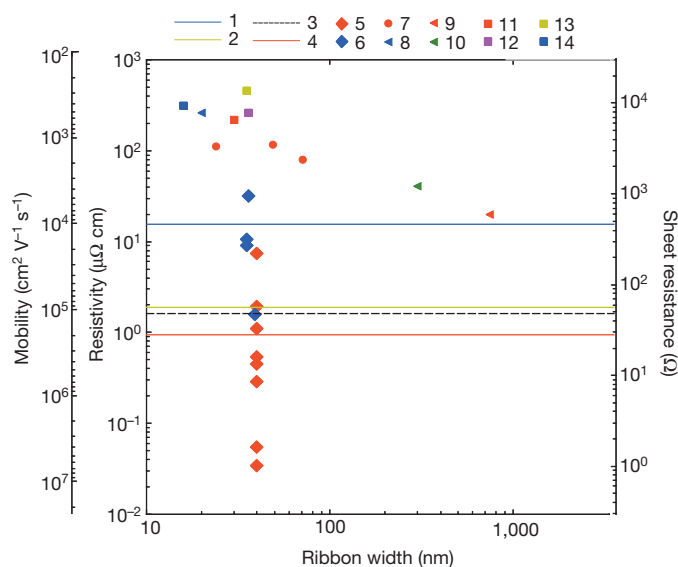


Figure 5 | Comparison with other work. Transport properties of epitaxial graphene nanoribbons reported here (5 and 6) are compared with exfoliated graphene as follows: 1, two-dimensional graphene on SiO₂ (ref. 25); 2, ultrahigh-mobility graphene on BN (ref. 26); 3, bulk silver; 4, the theoretical ideal graphene limit²⁵, and lithographically prepared graphene nanoribbons at a charge density $n_s = 10^{12} \text{ cm}^{-2}$ at $T = 30 \text{ K}$; 7, ref. 2; 8, ref. 4; 9, ref. 27; 10, ref. 28; 11, ref. 29; 12, ref. 3; 13, ref. 5; 14, ref. 30. Sheet resistances (R_{square}) for graphene ribbons are determined by multiplying reported resistances (in R_0 units) by W/L . For back-gated graphene, the resistivity at $V_g = V_D \pm 14 \text{ V}$ (corresponding to $n_s = \pm 10^{12} \text{ cm}^{-2}$) is reported, where V_D locates the Dirac point. Resistivities ρ correspond to $\rho = dR_{\text{square}}$, where $d = 3 \times 10^{-8} \text{ cm}$ corresponds to a monolayer thickness. Mobilities μ are determined from the definition $\mu = (n_s e R_{\text{square}})^{-1}$ at a charge density of 10^{12} cm^{-2} . For two-dimensional and bulk materials, bulk values are used (not adjusted for finite-size effects).

attributed to a rise of the chemical potential due to the magnetic field, then this implies that the charge carriers have magnetic moments of about $5\mu_B$ (see Supplementary Information). At room temperature, both channels apparently exhibit exponential resistance increases when their lengths increase beyond a threshold ($16 \mu\text{m}$ for the $0+$ mode and 160 nm for the $0-$ mode).

The properties of the ballistic modes are distinct from those of the other subbands ($|n| \geq 1$). Although the mean free paths of the $|n| \geq 1$ subbands (60 nm) are much larger than those observed in exfoliated graphene ribbons ($\sim 5 \text{ nm}$, see Supplementary Fig. 2), they are in line with those observed by others in two-dimensional graphene samples (Fig. 5). Clearly scattering mechanisms that apply to normal Dirac electrons do not apply to the ballistic modes discussed here. Because both modes have a conductance of $1G_0$ they probably represent distinct longitudinal modes of the $n = 0 \pm$ subbands (Fig. 3a), but they cannot both be derived from the same one-dimensional subband. Apparently the $n = 0+$ mode represents the ground-state longitudinal mode derived from the $n = 0+$ subband and the $n = 0-$ mode represents an excited state derived from the $n = 0-$ subband. The fact that properties of these two modes are so different is not expected and points to a broken symmetry. We emphasize that very similar properties are observed in carbon nanotubes²³ (Supplementary Information).

We have presented compelling evidence for single-channel ballistic transport in long epitaxial graphene nanoribbons. This implies that both spin and valley degeneracy is lifted. Moreover, exceptional transport is observed only in the $n = 0$ subband of the graphene ribbon and it is distinct from the behaviour of the $|n| \geq 1$ subbands that have much shorter mean free paths. We note that for exfoliated, lithographically patterned ribbons, the inverse is true: the $n = 0$ subbands have much shorter mean free paths than the $|n| \geq 1$ subbands, resulting in a

mobility gap. Consequently, the properties we observe are not simply the result of clean samples but possibly reflect correlation effects²⁴ that may be particularly important in the $n = 0$ subbands. Regardless of its origin, it likely that room-temperature ballistic transport will play an important part in future graphene nanoelectronics.

METHODS SUMMARY

For ribbons in Figs 2 and 3, trenches 20 nm deep were etched along the $[1\bar{1}00]$ direction. Samples in Fig. 2 were annealed at $1,600^\circ \text{C}$ for 15 min (ref. 7). Samples in Fig. 3 were heated at $1,300^\circ \text{C}$ in Ar ($4 \times 10^{-5} \text{ mbar}$), and then in UHV for 15 min at $1,100^\circ \text{C}$ (green dots, Fig. 3a) or at $1,150^\circ \text{C}$ (all others—see Supplementary Information). The natural-step ribbon⁷ (Fig. 1c and Fig. 4) was connected at each end to two 200-nm -deep graphitized trenches $1 \mu\text{m}$ apart that serve as current leads and voltage probes.

All ribbons were characterized with AFM, conducting AFM, SEM and electrostatic force microscopy, to determine ribbon widths and sidewall slopes (see ref. 7 for details, and also refs 6,15). The Soleil synchrotron facility (Cassiopée ARPES beam line) was used for graphene band structure measurements (Supplementary Fig. 1), to determine the number of graphene layers and the sidewall slopes^{7,16}.

Low-temperature ($T = 77 \text{ K}$) STM-STs measurements (Fig. 2) were performed (in Nancy) in a UHV chamber coupled to a preparation chamber. For STM, bias voltages are relative to the grounded tip. STs spectra were acquired with a PtIr tip ($V_{\text{bias}} = 70 \text{ mV}$, $1,100 \text{ Hz}$) and a lock-in current detection, in open feedback loop conditions.

The multi-probe measurements in Fig. 3 were performed in an Omicron Nano-probe UHV system (in Hannover), from 30 K to 300 K , using W tips positioned using a built-in SEM. The STs set point (Fig. 1d) was $2 \text{ V}/0.1 \text{ nA}$. The resistance between neighbouring ribbons was $>450 \text{ k}\Omega$ (Supplementary Fig. 11).

Results in Fig. 4 were obtained (in Atlanta) in a Janis variable temperature cryostat ($4\text{--}300 \text{ K}$) with a 9-T magnet, using standard low-frequency lock-in techniques (13 Hz , $100 \text{ nA} < I < 1 \mu\text{A}$). For $G(T)$, samples were cooled from 120 K to 4 K over 10 h , with a rate of two measurements per second.

Received 28 August; accepted 11 December 2013.

Published online 5 February 2014.

- Berger, C. *et al.* Ultrathin epitaxial graphite: 2D electron gas properties and a route toward graphene-based nanoelectronics. *J. Phys. Chem. B* **108**, 19912–19916 (2004).
- Han, M. Y., Özyilmaz, B., Zhang, Y. & Kim, P. Energy band-gap engineering of graphene nanoribbons. *Phys. Rev. Lett.* **98**, 206805 (2007).
- Han, M. Y., Brant, J. C. & Kim, P. Electron transport in disordered graphene nanoribbons. *Phys. Rev. Lett.* **104**, 056801 (2010).
- Chen, Z. H., Lin, Y. M., Rooks, M. J. & Avouris, P. Graphene nano-ribbon electronics. *Physica E* **40**, 228–232 (2007).
- Todd, K., Chou, H. T., Amasha, S. & Goldhaber-Gordon, D. Quantum dot behavior in graphene nanoconstrictions. *Nano Lett.* **9**, 416–421 (2009).
- Sprinkle, M. *et al.* Scalable templated growth of graphene nanoribbons on SiC. *Nature Nanotechnol.* **5**, 727–731 (2010).
- Ruan, M. *Structured Epitaxial Graphene for Electronics*. PhD thesis, Georgia Inst. Technol. (2012); available at <http://hdl.handle.net/1853/45596>.
- Castro Neto, A. H., Guinea, F., Peres, N. M. R., Novoselov, K. S. & Geim, A. K. The electronic properties of graphene. *Rev. Mod. Phys.* **81**, 109–162 (2009).
- Berger, C. *et al.* Electronic confinement and coherence in patterned epitaxial graphene. *Science* **312**, 1191–1196 (2006).
- Datta, S. *Electronic Transport in Mesoscopic Systems* (Cambridge Univ. Press, 1995).
- Nakada, K., Fujita, M., Dresselhaus, G. & Dresselhaus, M. S. Edge state in graphene ribbons: nanometer size effect and edge shape dependence. *Phys. Rev. B* **54**, 17954–17961 (1996).
- Wakabayashi, K., Takane, Y. & Sigrist, M. Perfectly conducting channel and universality crossover in disordered graphene nanoribbons. *Phys. Rev. Lett.* **99**, 036601 (2007).
- Frank, S., Poncharal, P., Wang, Z. L. & de Heer, W. A. Carbon nanotube quantum resistors. *Science* **280**, 1744–1746 (1998).
- de Heer, W. A. *et al.* Large area and structured epitaxial graphene produced by confinement controlled sublimation of silicon carbide. *Proc. Natl Acad. Sci.* **108**, 16900–16905 (2011).
- Hu, Y. *et al.* Structured epitaxial graphene: growth and properties. *J. Phys. D* **45**, 154010 (2012).
- Hicks, J. *et al.* A wide-bandgap metal-semiconductor-metal nanostructure made entirely from graphene. *Nature Phys.* **9**, 49–54 (2013).
- Norimatsu, W. & Kusunoki, M. Formation process of graphene on SiC (0001). *Physica E* **42**, 691–694 (2010).
- Büttiker, M. Four terminal phase coherent conductance. *Phys. Rev. Lett.* **57**, 1761–1764 (1986).
- de Picciotto, R., Stormer, H. L., Pfeiffer, L. N., Baldwin, K. W. & West, K. W. Four-terminal resistance of a ballistic quantum wire. *Nature* **411**, 51–54 (2001).

20. Tombros, N. *et al.* Quantized conductance of a suspended graphene nanoconstriction. *Nature Phys.* **7**, 697–700 (2011).
21. Huard, B. *et al.* Transport measurements across a tunable potential barrier in graphene. *Phys. Rev. Lett.* **98**, 236803 (2007).
22. Mott, N. F. Conduction in non-crystalline materials. III. Localized states in a pseudogap and near extremities of conduction and valence bands. *Phil. Mag.* **19**, 835–852 (1969).
23. Schonenberger, C., Bachtold, A., Strunk, C., Salvetat J. P. & Forro, L. Interference and interaction in multi-wall carbon nanotubes. *Appl. Phys. A* **69**, 283–295 (1999).
24. Das Sarma, S., Adam, S., Hwang, E. H. & Rossi, E. Electronic transport in two-dimensional graphene. *Rev. Mod. Phys.* **83**, 407–470 (2011).
25. Chen, J. H., Jang, C., Xiao, S. D., Ishigami, M. & Fuhrer, M. S. Intrinsic and extrinsic performance limits of graphene devices on SiO₂. *Nature Nanotechnol.* **3**, 206–209 (2008).
26. Mayorov, A. S. *et al.* Micrometer-scale ballistic transport in encapsulated graphene at room temperature. *Nano Lett.* **11**, 2396–2399 (2011).
27. Huard, B., Stander, N., Sulpizio, J. A. & Goldhaber-Gordon, D. Evidence of the role of contacts on the observed electron-hole asymmetry in graphene. *Phys. Rev. B* **78**, 121402R (2008).
28. Lemme, M., Echtermeyer, T. J., Baus, M. & Kurz, H. A graphene field effect device. *IEEE Electron Device Lett.* **28**, 282–284 (2007).
29. Lin, Y. M., Perebeinos, V., Chen, Z. H. & Avouris, P. Electrical observation of subband formation in graphene nanoribbons. *Phys. Rev. B* **78**, 161409(R) (2008).
30. Wang, X. R. *et al.* Graphene nanoribbons with smooth edges behave as quantum wires. *Nature Nanotechnol.* **6**, 563–567 (2011).

Supplementary Information is available in the online version of the paper.

Acknowledgements C.T. thanks the German Research Foundation Priority Program 1459 ‘Graphene’ for financial support. C.B., E.H.C. and W.A.d.H. thank R. Dong, P. Goldbart, Z. Guo, J. Hankinson, J. Hicks, Y. Hu, J. Kunc, M. Kindermann, D. Mayou, M. Nevius, J. Palmer, A. Sidorov and P. de Heer for assistance and comments. C.B., E.H.C. and W.A.d.H. thank the AFOSR, NSF (MRSEC – DMR 0820382), W. M. Keck Foundation and Partner University Fund for financial support. Work at ORNL was supported by the Scientific User Facilities Division, BES of the DOE.

Author Contributions J.B. and F.E. produced samples and performed the *in situ* transport experiments in Hannover relating to Fig. 3. C.T. performed and supervised the transport experiments in Fig. 3, discussed the data and commented on the paper. M.R. produced the samples and performed transport experiments shown in Fig. 4 and Supplementary Figs 3–6. E.H.C., A.T. and A.T.-I. performed ARPES experiments, and A.T. and M.S. the STM and STS experiments. Z.J. performed confirming spin transport measurements and contributed to C-AFM results shown in Supplementary Fig. 6b. A.-P.L. performed earlier SPM measurements. W.A.d.H. conceived and supervised the experiment and interpreted the data. C.B. supervised and performed the Atlanta based experiments. W.A.d.H. and C.B. wrote the paper.

Author Information Reprints and permissions information is available at www.nature.com/reprints. The authors declare no competing financial interests. Readers are welcome to comment on the online version of the paper. Correspondence and requests for materials should be addressed to W.A.d.H. (walt.deheer@physics.gatech.edu).